

Wannier-Stark states of graphene monolayer in strong electric field

Hamed Koochaki Kelardeh¹, Vadym Apalkov¹, and Mark I. Stockman^{1,2,3}

¹*Department of Physics and Astronomy, Georgia State University, Atlanta, Georgia 30303, USA*

²*Fakultät für Physik, Ludwig-Maximilians-Universität,*

Geschwister-Scholl-Platz 1, D-80539 München, Germany

³*Max-Planck-Institut für Quantenoptik, Hans-Kopfermann-Strasse 1, D-85748 Garching, Germany*

(Dated: December 6, 2024)

We study theoretically the Wannier-Stark energy spectra of graphene monolayer in strong uniform electric field within the tight-band model of graphene. The tight-binding model captures both the energy dispersion of the conduction and valence bands of graphene and the corresponding interband coupling. Within a single band, a constant electric field produces quantized equidistant energy levels (Wannier-Stark ladder), separated by Bloch frequency. The interband coupling results in mixing of the states of different bands and anticrossing of corresponding levels. Near the Dirac points, the Wannier-Stark energy spectrum is determined by specific wave vector dependence of the interband coupling. Such coupling has sharp peaks near the Dirac points. Due to this property, the Wannier-Stark energy spectra of two-band graphene system can be found analytically. In this case, the anticrossing gaps, expressed in the units of the Bloch frequency, have the same value at all anticrossing points.

I. INTRODUCTION

The dynamics of an electron in periodic potential and external electric field is characterized by Bloch oscillations[1], which is a feature of the intraband electron dynamics, and Zener tunneling[2], which is related to interband coupling. The Bloch oscillations occur due to acceleration of an electron by electric field, which, in the reciprocal space, is described by the "acceleration theorem", and subsequent Bragg reflection from the periodic lattice potential at the boundaries of the first Brillouin zone. The interference of electron wave packet, following such periodic dynamics in the reciprocal space, results in Wannier-Stark (WS) localization of an electron in the coordinate space and in the formation of the Wannier-Stark states[3, 4]. These states originating from a given band are separated by the Bloch oscillation frequency [1] and form the WS ladder. The Bloch oscillations and corresponding WS states have been observed experimentally in semiconductor superlattices[5–9] and recently the Bloch oscillations were reported as oscillations in the waveform of intense terahertz pulse propagating through GaSe crystal[10].

The external electric field not only modifies the intraband electron dynamics, resulting in formation of the WS states, but also introduces interband coupling of the states of different bands. Such coupling can be described in terms of the Zener tunneling, which results in a finite width of the WS levels of individual band[11–14], or in terms of coupling of the WS states of different bands, which results in mixing of corresponding WS states. The strongest mixing is realized when the energies of the WS levels of different bands are equal. As a function of electric field, at these points the system show anticrossing behavior. In time-dependent electric field, e.g., in the electric field of the optical pulse, it is convenient to utilize the notion of the anticrossing points to describe the time-dependent electron dynamics. The electron dynam-

ics in this case can be described as an adiabatic formation of WS states of different bands and then as a dynamics of passage of anticrossing points of these states. Depending on relation between the anticrossing gap and the rate of change of the electric field, the dynamics of passage of the anticrossing points can be adiabatic or diabatic[15]. Such description of electron dynamics in time-dependent electric field was successfully used for interpretation of experimental results on interaction of ultrashort intense optical pulses with dielectrics[16, 17].

Description of interaction of time-dependent electric field, e.g., optical pulse, with a solid in terms of the dynamics of passage of anticrossing points requires knowledge of both the positions of the anticrossing points and the magnitudes of the corresponding anticrossing gaps. These parameters depend on the band structure of the solid and on the strength of the interband coupling. Below we study the properties of the WS states of monolayer graphene with potential application of this knowledge to the description of interaction of strong time-dependent electric field with electrons in graphene. Graphene monolayer[18–20] has honeycomb 2D crystal structure, which is characterized by unique energy dispersion relation. Namely, the low energy excitations are gapless and are described by the Dirac relativistic massless equation with two Dirac cones. Another important feature of the relativistic energy dispersion is singularity of the interband dipole matrix element between the valence and conduction bands at the Dirac points. In this case, the corresponding interband coupling, introduced by an electric field, is localized in the reciprocal space at the discrete Dirac points. Below we show that, due to this property, the stationary Schrödinger equation in a constant electric field can be solved exactly within the nearest neighbor tight-binding model of graphene for rational directions of the electric field. The WS energy spectra of an electron on honeycomb lattice was studied in Ref. [21] in the tight-binding approximation for both

rational and irrational directions of the electric field. It was shown that, at a given electric field with rational direction, the spectrum has a band structure with infinite number of equally spaced energy bands. In the present paper, we study the properties of the energy spectra as a function of electric field. In this case, we concentrate on the parameters of the anticrossing points. Namely, we determine the positions of the anticrossing points and the corresponding anticrossing gaps. Near the Dirac points, we obtain analytical expressions for these parameters.

II. MAIN EQUATIONS

The WS states of an electron in graphene are defined as electron states in periodic lattice potential of graphene and in constant external electric field. Thus the WS state can be found as a solution of the following Schrödinger equation

$$E\Psi = \mathcal{H}\Psi, \quad (1)$$

where \mathcal{H} is a single-particle Hamiltonian, which has the form

$$\mathcal{H} = \mathcal{H}_0 + e\mathbf{F}\mathbf{r}. \quad (2)$$

Here \mathcal{H}_0 is a single electron Hamiltonian of graphene, which determines the electron dynamics in periodic lattice potential of graphene, $\mathbf{r} = (x, y)$ is a 2D vector, e is the electron charge, and $\mathbf{F} = [F \cos \theta, F \sin \theta]$ is the external constant electric field with the magnitude F and the direction, determined by angle θ relative to the x axis - see Fig. 1(b).

We describe the electron states in graphene within the nearest neighbor tight-binding model [22–25] with the tight-binding coupling between the sites of two sublattices "A" and "B" of graphene crystal structure - see Fig. 1(a). Such model describes both the conduction and valence bands of graphene and captures the properties of the Dirac points. In the reciprocal space the tight-binding Hamiltonian \mathcal{H}_0 is a 2×2 matrix of the form [22, 23]

$$\mathcal{H}_0 = \begin{pmatrix} 0 & \gamma f(\mathbf{k}) \\ \gamma f^*(\mathbf{k}) & 0 \end{pmatrix}, \quad (3)$$

where $\gamma = -3.03$ eV is the hopping integral and

$$f(\mathbf{k}) = \exp\left(i\frac{ak_x}{\sqrt{3}}\right) + 2 \exp\left(-i\frac{ak_x}{2\sqrt{3}}\right) \cos\left(\frac{ak_y}{2}\right). \quad (4)$$

Here $a = 2.46\text{\AA}$ is a lattice constant. The energy spectrum of Hamiltonian \mathcal{H}_0 consists of conduction band (π^* or anti-bonding band) and valence bands (π or bonding band) with the energy dispersion $E_c(\mathbf{k}) = -\gamma|f(\mathbf{k})|$ (conduction band) and $E_v(\mathbf{k}) = \gamma|f(\mathbf{k})|$ (valence band). Such energy dispersion is shown in Fig. 1(c) and consists of two inequivalent sets of Dirac points (cones) \mathbf{K} and

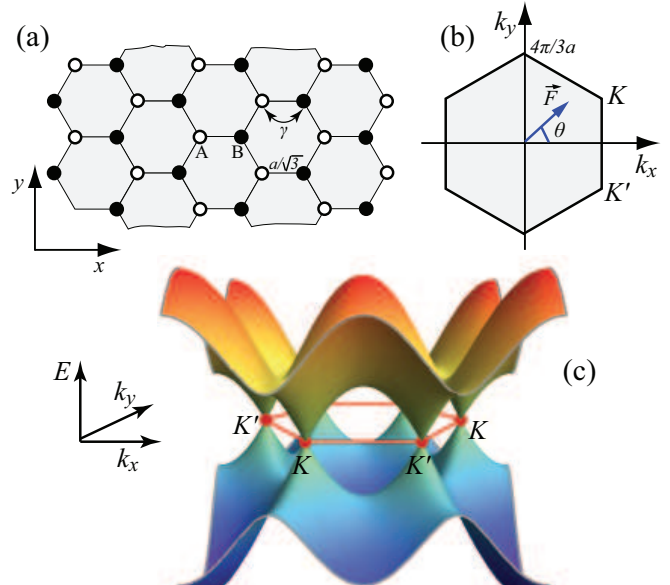


FIG. 1: (a) Honeycomb lattice structure of 2D graphene, which consists of two sublattices with atoms labeled by "A" (open circles) and "B" (filled circles), respectively. The nearest neighbor coupling with hopping integral γ is also shown. (b) The first Brillouin zone of graphene. Points K and K' are two inequivalent Dirac points, which correspond to two valleys of low energy spectrum of graphene. The direction of electric field is shown by blue line and is characterized by angle θ relative to the x axis. (c) Energy dispersion of graphene within the nearest neighbor tight-binding model. The K and K' Dirac points are labeled. The conduction and the valence bands correspond to positive and negative energies, respectively.

\mathbf{K}' . The corresponding wave functions of the conduction and valence bands are

$$\Psi_{\mathbf{k}}^{(c)}(\mathbf{r}) = \frac{e^{i\mathbf{k}\mathbf{r}}}{\sqrt{2}} \begin{pmatrix} 1 \\ e^{i\phi_{\mathbf{k}}} \end{pmatrix} \quad (5)$$

and

$$\Psi_{\mathbf{k}}^{(v)}(\mathbf{r}) = \frac{e^{i\mathbf{k}\mathbf{r}}}{\sqrt{2}} \begin{pmatrix} -1 \\ e^{i\phi_{\mathbf{k}}} \end{pmatrix}, \quad (6)$$

where $f(\mathbf{k}) = |f(\mathbf{k})|e^{i\phi_{\mathbf{k}}}$. The wave functions $\Psi_{\mathbf{k}}^{(c)}$ and $\Psi_{\mathbf{k}}^{(v)}$ have two components corresponding to two sublattices A and B.

Taking the eigenfunctions $\Psi_{\mathbf{k}}^{(v)}$ and $\Psi_{\mathbf{k}}^{(c)}$ of Hamiltonian \mathcal{H}_0 as a basis, we express the general solution of the Schrödinger equation (1) in the form

$$\Psi(\mathbf{r}) = \sum_{\mathbf{k}} \left[\phi_v(\mathbf{k})\Psi_{\mathbf{k}}^{(v)}(\mathbf{r}) + \phi_c(\mathbf{k})\Psi_{\mathbf{k}}^{(c)}(\mathbf{r}) \right]. \quad (7)$$

The expansion coefficients $\phi_v(\mathbf{k})$ and $\phi_c(\mathbf{k})$ satisfy the following eigenvalue equation

$$E\phi_v(\mathbf{k}) = E_v(\mathbf{k})\phi_v(\mathbf{k}) + ie\mathbf{F}\frac{d\phi_v(\mathbf{k})}{d\mathbf{k}} + \mathbf{F}\mathbf{D}(\mathbf{k})\phi_c(\mathbf{k}) \quad (8)$$

$$E\phi_c(\mathbf{k}) = E_c(\mathbf{k})\phi_c(\mathbf{k}) + ie\mathbf{F}\frac{d\phi_c(\mathbf{k})}{d\mathbf{k}} + \mathbf{F}\mathbf{D}(\mathbf{k})\phi_v(\mathbf{k}) \quad (9)$$

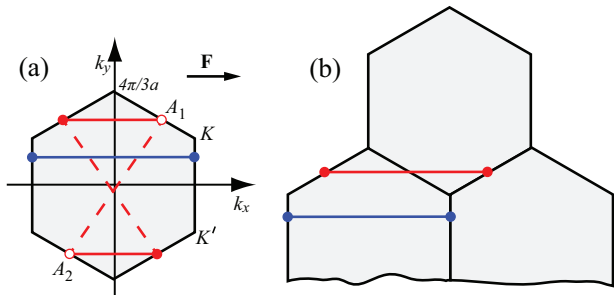


FIG. 2: The electron states of the reciprocal space, which are coupled by a constant electric field parallel to the x axis, are shown by solid lines of two different colors (red and blue), where different colors correspond to two different values of k_y . (a) The coupled states are shown in the first Brillouin zone. The equivalent points (at the edges of the Brillouin zone) are shown by the same type of points, i.e. solid red points or open red points. The equivalent points are connected by a vector of reciprocal lattice. (b) The coupled states are shown in the whole reciprocal space. The first Brillouin zones, localized at different points of the reciprocal lattice, are also shown. The equivalent points, which are connected by a vector of reciprocal lattice, are shown by the same type of points, e.g., two red points are equivalent.

where $\mathbf{D}(\mathbf{k}) = [D_x(\mathbf{k}), D_y(\mathbf{k})]$ is the dipole matrix element between the conduction and valence band states with the wave vector \mathbf{k} , i.e.

$$\mathbf{D}(\mathbf{k}) = \langle \Psi_{\mathbf{k}}^{(c)} | e\mathbf{r} | \Psi_{\mathbf{k}}^{(v)} \rangle. \quad (10)$$

Substituting the conduction and valence band wave functions (5) and (6) into Eq. (10), we obtain the following expressions for the interband dipole matrix elements

$$D_x(\mathbf{k}) = \frac{ea}{2\sqrt{3}} \frac{1 + \cos\left(\frac{ak_y}{2}\right) \left[\cos\left(\frac{3ak_x}{2\sqrt{3}}\right) - 2 \cos\left(\frac{ak_y}{2}\right) \right]}{1 + 4 \cos\left(\frac{ak_y}{2}\right) \left[\cos\left(\frac{3ak_x}{2\sqrt{3}}\right) + \cos\left(\frac{ak_y}{2}\right) \right]} \quad (11)$$

and

$$D_y(\mathbf{k}) = \frac{ea}{2} \frac{\sin\left(\frac{ak_y}{2}\right) \sin\left(\frac{3ak_x}{2\sqrt{3}}\right)}{1 + 4 \cos\left(\frac{ak_y}{2}\right) \left[\cos\left(\frac{3ak_x}{2\sqrt{3}}\right) + \cos\left(\frac{ak_y}{2}\right) \right]}. \quad (12)$$

Solution of the system of equations (8)-(9) satisfies periodic boundary condition in the reciprocal space with the periodicity of reciprocal lattice vectors. From this condition the WS energy spectrum is obtained.

The system (8)-(9) is the system of the first order differential equations, where constant electric field introduces both interband and intraband coupling of the electron states. The interband coupling is realized only between the states with the same wave vector, while the intraband coupling occurs only between the states laying in the reciprocal space on a line, the orientation of which is determined by the direction of electric field. These

lines can be identified by considering electron dynamics in a reciprocal space and in a constant electric field. If an electron is initially at some point \mathbf{k} of the reciprocal space and a constant electric field is applied, then the electron will drift along the direction of electric field following the acceleration theorem, $d\mathbf{k}/dt = e\mathbf{F}/m\hbar$, and experiencing Bragg-scattering at the boundaries of the Brillouin zone. Then the corresponding electron trajectory determines the line of coupled states.

The intraband-coupled states can be described by considering the states either in the first Brillouin zone only or in the whole reciprocal space. In both cases the equivalence of the points connected by a vector of reciprocal lattice should be taken into account. Such equivalence determines the periodic boundary conditions in the reciprocal space, from which the energy spectrum can be obtained.

First, we assume that the electric field is parallel to the x axis. In this case, the lines of coupled states are also parallel to axis x and are parametrized by the y component of the wave vector, k_y . In Fig. 2 the states coupled by such electric field are shown in the first Brillouin zone [Fig. 2(a)] and in the whole reciprocal space [Fig. 2(b)]. In the first Brillouin zone we need to take into account the equivalence of the points connected by a vector of the reciprocal lattice, e.g., points A_1 and A_2 are equivalent. In Fig. 2, two sets of coupled states (lines) corresponding to different values of k_y are shown. If $k_y < 2\pi/a$ then the typical line of coupled states is shown by a blue solid line in Fig. 2. The solid blue points at the ends of the line are coupled by a vector of reciprocal lattice, which determine the periodic boundary conditions for the wave functions $\phi_v(\mathbf{k})$ and $\phi_c(\mathbf{k})$, i.e., $\phi_v(-2\pi/a\sqrt{3}, k_y) = \phi_v(2\pi/a\sqrt{3}, k_y)$ and $\phi_c(-2\pi/a\sqrt{3}, k_y) = \phi_c(2\pi/a\sqrt{3}, k_y)$. From these conditions the energy spectrum is obtained.

If $k_y > 2\pi/3a$, then the line of coupled states in the first Brillouin zone consists of two line segments, which are shown by red solid lines in Fig. 2(a). These line segments have two sets of equivalent points: solid red points and open red points. The points in each set are connected by the corresponding vector of the reciprocal lattice.

In the whole reciprocal space, the part of which is shown in Fig. 2(b), the lines, which describe the coupled states, are straight lines for both $k_y < 2\pi/3a$ and $k_y > 2\pi/3a$. For the case $k_y > 2\pi/3a$, the line of coupled states is located in two first Brillouin zones – see Fig. 2(b). For both the red and blue lines the end points of the lines are connected by the same vector of reciprocal lattice, $\mathbf{G} = (4\pi/a\sqrt{3}, 0)$, which makes the end points of the lines equivalent points and introduces periodic boundary conditions for the system of equations (8)-(9).

III. RESULTS AND DISCUSSION

A. Wannier-Stark levels of a single band

Without interband coupling, i.e. $\mathbf{D} = 0$, the equations (8)-(9) becomes decoupled. For a single band, e.g., valence band, Eq. (8) becomes

$$E\phi_v(\mathbf{k}) = E_v(\mathbf{k})\phi_v(\mathbf{k}) + ieF\frac{d\phi_v(\mathbf{k})}{dk_x}, \quad (13)$$

where the electric field is parallel to the x axis. Solution of the first order differential equation (13) has the form

$$\phi_v^{(0)}(\mathbf{k}) = \frac{1}{\sqrt{2k_0}} \exp \left[-\frac{i}{eF} \left(E(k_x + k_0) - \int_{-k_0}^{k_x} E_v(k', k_y) dk' \right) \right], \quad (14)$$

where we introduced the following notation $k_0 = 2\pi/a\sqrt{3}$. From periodicity of the wave function $\phi_v(-k_0, k_y) = \phi_v(k_0, k_y)$ we obtain the WS energy spectrum

$$E_{v,n}^{WS} = E_{v,0}(k_y) + \hbar\omega_B n, \quad (15)$$

where n is integer and the band offset $E_{v,0}(k_y)$ is

$$E_{v,0}(k_y) = \frac{1}{2k_0} \int_{-k_0}^{k_0} E_v(k', k_y) dk'. \quad (16)$$

The Bloch frequency ω_B in Eq. (15) is defined as

$$\omega_B = \frac{eF}{2k_0\hbar}. \quad (17)$$

The energy spectrum (15) forms the WS ladder with equidistant energy levels.

For conduction band, the energy spectrum has a similar form,

$$E_{c,n}^{WS} = E_{c,0}(k_y) + \hbar\omega_B n, \quad (18)$$

with the corresponding band offset

$$E_{c,0}(k_y) = \frac{1}{2k_0} \int_{-k_0}^{k_0} E_c(k', k_y) dk'. \quad (19)$$

For the tight-binding model, introduced above, there is a relation $E_{c,0}(k_y) = -E_{v,0}(k_y)$. The wave functions of the WS levels of the conduction band are

$$\phi_c^{(0)}(\mathbf{k}) = \frac{1}{\sqrt{2k_0}} \exp \left[-\frac{i}{eF} \left(E(k_x + k_0) - \int_{-k_0}^{k_x} E_c(k', k_y) dk' \right) \right], \quad (20)$$

In the coordinate space, the WS levels are localized and the integer index n determines the center of localization.

B. Wannier-Stark states of two-band model: analytical results

1. Energy spectrum

The interband coupling, described by the dipole matrix elements $\mathbf{D}(\mathbf{k})$, has a strong dependence on the wave vector \mathbf{k} . Near the Dirac points (K and K' points in Fig. 1) the dipole matrix elements have sharp peaks. The dependence of the dipole matrix element D_x on the wave vector k_x for different values of k_y is shown in Fig. 3. The Dirac point is at $\mathbf{K} = (K_x, K_y) = (2\pi/a)(1/\sqrt{3}, 1/3)$, i.e. it corresponds to $k_y = K_y = (1/3)(2\pi/a) = k_0/\sqrt{3}$ and $k_x = K_x = (2\pi/a\sqrt{3}) = k_0$. Away from the Dirac point, i.e. when k_y is close to zero and far from $(1/3)(2\pi/a)$ [see Fig. 3(a)], the dipole matrix element, $|D_x|$, has a broad maximum near $k_x = k_0$. With increasing k_y the maximum becomes more pronounced. Near the Dirac point, [see, for example, the case of $k_y = 0.33(2\pi/a)$ in Fig. 3(b)], the dipole matrix element $|D_x|$ has a sharp peak at $k_x = K_x = k_0$. Near this peak the dipole matrix element $D_x(k_x, k_y)$ behaves as

$$D_x(k_x, k_y) \approx \frac{3ea}{4\pi} \left[-\frac{1}{\delta_y} + \frac{3}{\delta_y^2} \delta_x^2 \right], \quad (21)$$

where $\delta_y = (k_y - K_y)/K_y$ and $\delta_x = (k_x - K_x)/K_x$. Thus, for a given k_y , the maximum value of the dipole matrix element is $\frac{3ea}{4\pi} [K_y/(k_y - K_y)]$, which diverges at $k_y \rightarrow K_y$.

Although the shape of $D_x(k_x, k_y)$ as a function of k_x depends on the value of the y component of the wave vector k_y , the "net" interband coupling, which can be characterized by the integral

$$D_x^{(net)}(k_y) = \int_{-k_0}^{k_0} D_x(k_x, k_y) dk_x, \quad (22)$$

does not depend on k_y . Namely, one can show that the net coupling is $D_x^{(net)}(k_y) = -e\pi/3$ for all values of k_y .

A strong dependence of the dipole matrix element on k_x near the Dirac point, which is illustrated in Fig. 3 and is supported by Eq. (21), can be approximated by the δ -function, i.e.

$$D_x(k_x, k_y) = e\Lambda_0\delta(k_x - k_0). \quad (23)$$

Here the strength Λ_0 of the δ -function is determined by condition that the net dipole coupling [see Eq. (22)] in both cases, i.e., exact expression for the dipole matrix element and the δ -function approximation, is the same. Then $\Lambda_0 = -\pi/3$.

For the δ -function profile of the dipole matrix elements, the system of equations (8)-(9) can be solved analytically. Such solution can be obtained as follows. We are looking for a solution of the system of equation (8)-(9) within a line segment $0 \leq k_x < 2k_0$ with periodical boundary conditions (Here, it is convenient to consider the interval

$0 \leq k_x < 2k_0$ and not the interval $-k_0 \leq k_x < k_0$ introduced before). The dipole matrix element is non-zero only at $k_x = k_0$. Then for $0 \leq k_x < k_0$ and $k_0 < k_x < 2k_0$ there is no interband coupling between the valence and conduction bands. Within these intervals the general solution of the system (8)-(9) takes the form

$$\phi_v(\mathbf{k}) = A_1 e^{-i(\epsilon F)^{-1} (E k_x - \int_0^{k_x} E_v(k', k_y) dk')} \quad (24)$$

$$\phi_c(\mathbf{k}) = A_2 e^{-i(\epsilon F)^{-1} (E k_x - \int_0^{k_x} E_c(k', k_y) dk')} \quad (25)$$

at $0 \leq k_x < k_0$ and

$$\phi_v(\mathbf{k}) = B_1 e^{-i(\epsilon F)^{-1} (E k_x - \int_0^{k_x} E_v(k', k_y) dk')} \quad (26)$$

$$\phi_c(\mathbf{k}) = B_2 e^{-i(\epsilon F)^{-1} (E k_x - \int_0^{k_x} E_c(k', k_y) dk')} \quad (27)$$

at $k_0 < k_x < 2k_0$. Here A_1 , A_2 , B_1 , and B_2 are constants. At point $k_x = k_0$ the δ -function dipole matrix element (23) introduces the following relation between the values of the wave function at $k_x = k_0 - 0$ and $k_x = k_0 + 0$

$$\phi_v|_{k_0+0} = -i\phi_c|_{k_0-0} \sin \Lambda_0 + \phi_v|_{k_0-0} \cos \Lambda_0 \quad (28)$$

$$\phi_c|_{k_0+0} = \phi_c|_{k_0-0} \cos \Lambda_0 - i\phi_v|_{k_0-0} \sin \Lambda_0 \quad (29)$$

Thus the δ -function coupling results in rotation of a pseudospin, associated with two components of the wave function, by a finite angle Λ_0 .

Substituting expressions (24)-(27) into relations (28)-(29) and taking into account the periodic boundary conditions, we obtain an equation on the energy spectrum of the WS states

$$\cos\left(\frac{2k_0}{eF}E\right) = \cos(\Lambda_0) \cos\left(\frac{2k_0}{eF}E_{c,0}(k_y)\right), \quad (30)$$

where we took into account the relation $E_{c,0} = -E_{v,0}$, which is valid within tight-binding model introduced above. Solution of Eq. (30) is parametrized by an integer number n and has the form

$$E_n^{(\pm)} = \pm \frac{eF}{2k_0} \left\{ \cos^{-1} \left[\cos \Lambda_0 \cos \left(\frac{2k_0}{eF} E_{c,0}(k_y) \right) \right] + 2\pi n \right\}. \quad (31)$$

Here the positive and negative signs correspond to the energy spectra of the conduction ($E_n^{(+)}$) and valence ($E_n^{(-)}$) bands, respectively.

It is convenient to rewrite Eq. (31) in the dimensionless energy variables, $\varepsilon_n^{(\pm)} = E_n^{(\pm)}/\hbar\omega_B = E_n^{(\pm)}(2k_0/eF)$ and $\varepsilon_{c,0} = E_{c,0}(k_y)/\hbar\omega_B = E_{c,0}(2k_0/eF)$. Then Eq. (31) takes form

$$\varepsilon_n^{(\pm)} = \pm \cos^{-1} [\cos \Lambda_0 \cos \varepsilon_{c,0}] + 2\pi n. \quad (32)$$

The corresponding dimensionless energy spectrum is shown in Fig. 4(a). The anticrossing points of the energy levels can be clearly identified. Such points are related to the anticrossing of the WS ladders of different bands, i.e. conduction and valence bands. The anticrossing points can be labeled by an integer number $l = 1, 2, \dots$. In

dimensionless variables, the positions of the anticrossing points are

$$\varepsilon_{c,0}^{(l)} = l\pi, \quad (33)$$

or in terms of the electric field, the anticrossing points are at

$$F^{(l)} = \frac{2k_0}{e\pi l} E_{c,0}. \quad (34)$$

The positions of the anticrossing points can be also estimated from the expressions (15), (18) for the energies of the WS states of uncoupled conduction and valence bands. For uncoupled bands, the anticrossing points are determined by equation $E_{c,n_c}^{WS} = E_{v,n_v}^{WS}$. From this expression, one can derive the positions of the anticrossing points at

$$F_{\text{uncoupled}}^{(l)} = \frac{4k_0}{e l} E_{c,0}, \quad (35)$$

where $l = n_c - n_v$. Comparing the exact expression (34) and approximation (35), we can conclude that the interband coupling strongly renormalizes the positions of the anticrossing points,

$$F^{(l)} = F_{\text{uncoupled}}^{(l)}/(2\pi) \approx F_{\text{uncoupled}}^{(l)}/6.3, \quad (36)$$

i.e. the interband coupling moves the anticrossing points to smaller values of the electric field. This behavior is opposite to what we observe for the positions of the anticrossing points in two-band model of dielectric, where the interband coupling moves the anticrossing points to the higher values of electric field[15].

In the dimensionless units, the anticrossing gaps are the same for all anticrossing points [see Fig. 4(a)]. The value of the dimensionless gap, $\Delta_g/\hbar\omega_B$, can be found as the difference between the corresponding energy levels, $\Delta_g/\hbar\omega_B = \varepsilon_1^{(-)} - \varepsilon_0^{(+)}$, calculated at a point $\varepsilon_{c,0} = \pi$. Then

$$\Delta_g/\hbar\omega_B = 2\Lambda_0. \quad (37)$$

In the original units, the anticrossing gap corresponding to the anticrossing point with index l [see Eq. (33)] takes the form

$$\Delta_g^{(l)} = \frac{2\Lambda_0}{l\pi} E_{c,0}. \quad (38)$$

Since the dimensionless parameter $\varepsilon_{c,0}$ is inversely proportional to electric field, then in the energy spectrum, considered as a function of electric field, the anticrossing point with index $l = 1$ is the last anticrossing point [see Fig. 4(a)]. In Fig. 4(b) the energy spectrum, calculated from Eq. (31), is shown as a function of electric field. The anticrossing points with indexes $l = 1$ and $l = 2$ are also marked. The corresponding anticrossing gaps are given by Eq. (38). The last anticrossing points with index $l = 1$ has the largest anticrossing gap, $\Delta_g^{(1)} = 2\Lambda_0 E_{c,0}/\pi$.

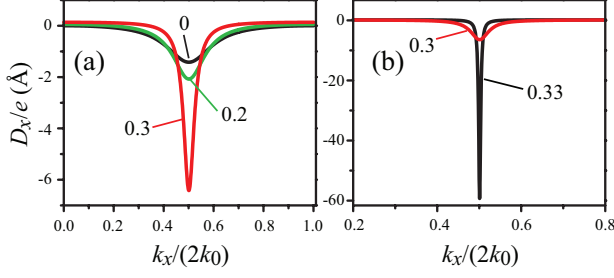


FIG. 3: The dipole matrix elements D_x are shown as a function of k_x for different values of k_y . The wave vector k_x is measured in units of $2k_0$, where $k_0 = 2\pi/a\sqrt{3}$. The Dirac point is at $k_x = k_0$ and $k_y = k_0/\sqrt{3} = (1/3)(2\pi/a)$. The numbers near the lines are the values of k_y in units of $(2\pi/a)$.

For graphene, within the tight binding model introduced above, the parameter Λ_0 , calculated at $k_y = k_{y,0} = 2\pi/3a$, is $|\Lambda_0| = \pi/3 \approx 1.05$. For this value of $k_y = k_{y,0}$, the energy dispersion is

$$E_c(k_x, k_{y,0}) = -2\gamma \cos\left(\frac{\sqrt{3}ak_x}{4}\right). \quad (39)$$

Then the band offset of the conduction band, defined by Eq. (19), is

$$E_{c,0}(k_{y,0}) = -\frac{4\gamma}{\pi} \approx 3.86\text{eV}. \quad (40)$$

For these values of Λ_0 and $E_{c,0}$, we obtain from Eqs. (34) and (38) the positions of the anticrossing points and corresponding anticrossing gaps

$$F^{(l)} = \frac{8k_0|\gamma|}{e\pi^2 l} \approx \frac{3.59}{l} \left(\frac{\text{V}}{\text{\AA}}\right), \quad (41)$$

$$\Delta_g^{(l)} = \frac{8|\gamma|}{3\pi l} \approx \frac{2.54}{l} (\text{eV}). \quad (42)$$

The anticrossing at $l = 1$ corresponds to the last anticrossing, i.e., maximum electric field of 3.59 V/\AA . The anticrossing gap at this point is 2.54 eV .

2. Wave functions

The wave functions of the WS states of the two-band graphene model have two components $\phi_v(\mathbf{k})$ and $\phi_c(\mathbf{k})$, which give the amplitudes of the wave functions in the valence and conduction bands, respectively. The functions $\phi_v(\mathbf{k})$ and $\phi_c(\mathbf{k})$ are determined by Eqs. (24)-(27), where the unknown coefficients A_1 , A_2 , B_1 , and B_2 can be found from the boundary conditions (28)-(29) and at a given energy of the WS state E , have the following form

$$A_2 = A_1 e^{-i(\epsilon F)^{-1} \int_0^{2k_0} (E_c(k', k_y) - E) dk'} \quad (43)$$

$$B_1 = i \frac{A_2 - A_1 \cos(\Lambda_0)}{\sin(\Lambda_0)} \quad (44)$$

$$B_2 = B_1 \cos(\Lambda_0) - i A_1 \sin(\Lambda_0). \quad (45)$$

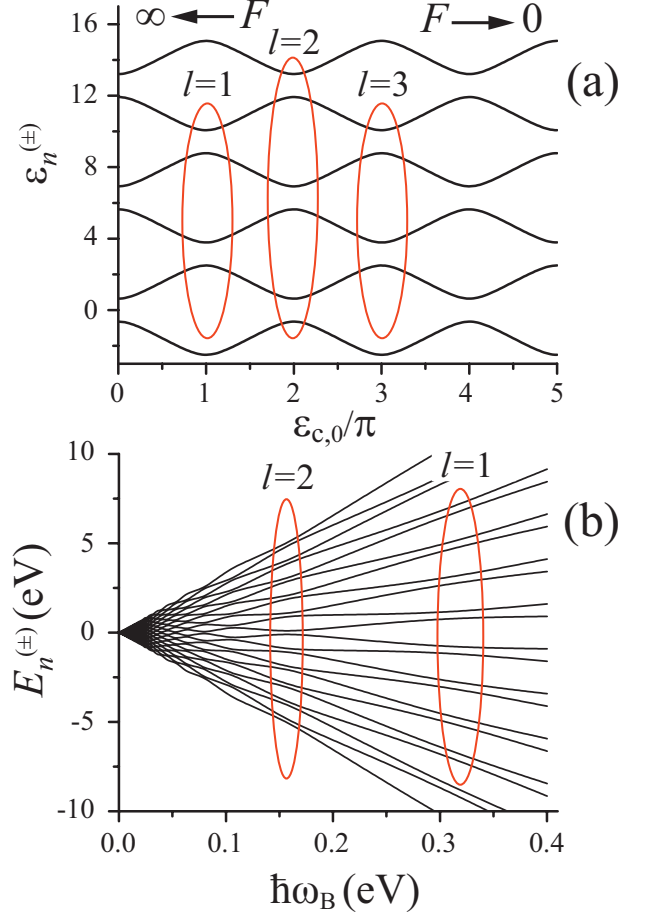


FIG. 4: (a) Dimensionless energies $\varepsilon_n^{(\pm)}$ of the WS states, calculated from Eq. (32), are shown as a function of dimensionless parameter $\varepsilon_{c,0}$ for different values of integer number n . Parameter Λ_0 is $\Lambda_0 = 0.6$. Different types of anticrossing points are labeled by integer parameter l . With increasing electric field, the last anticrossing point corresponds to $l = 1$ and occurs at $\varepsilon_{c,0} = \pi$. (b) The energies $E_n^{(\pm)}$ of the WS states, calculated from Eq. (31), are shown as a function of Bloch frequency, $\hbar\omega_B$, which is proportional to electric field. The anticrossing points, corresponding to $l = 1$ and $l = 2$, are marked by red lines. The parameter Λ_0 is $\Lambda_0 = 0.6$, and $E_{c,0} = 1 \text{ eV}$.

Here the coefficient A_1 can be found from normalization condition. The wave functions $(\phi_v(\mathbf{k}), \phi_c(\mathbf{k}))$ determine the electron amplitudes in the reciprocal space. The corresponding wave functions in the direct coordinate space are determined by the 1D Fourier transform

$$\tilde{\phi}_v(x, k_y) = \int dx \phi_v(k_x, k_y) e^{ik_x x}, \quad (46)$$

$$\tilde{\phi}_c(x, k_y) = \int dx \phi_c(k_x, k_y) e^{ik_x x}, \quad (47)$$

where we consider the spatial dependence of the wave function along axis x only, i.e. along the direction of electric field. In this case, the y component of the wave

vector, k_y , should be considered as a parameter.

Without interband coupling, i.e., at $\Lambda_0 = 0$, and at $k_y = k_{y,0}$, the WS wave functions for a given band, e.g., conduction band, can be expressed in terms of the Bessel functions,

$$\tilde{\phi}_c(x, k_y) \propto J_{\left| \frac{4}{\sqrt{3}a} \left(x - \frac{E}{eF} \right) \right|} \left(\frac{\gamma}{\hbar\pi\omega_B} \right), \quad (48)$$

where $J_n(z)$ is the Bessel function of order n and the Bloch frequency is given by Eq. (17). Such analytical expression is obtained for the energy dispersion (39). The wave function (48) is localized in the x -space at a point $x = E/eF$, which is determined by the energy of the WS state.

The interband coupling Λ_0 results in mixing of the wave functions of different (conduction and valence) bands. The mixing is the strongest at the anticrossing points and the resulting WS wave functions are also localized similar to one-band approximation (48). Such wave functions are given by Eqs. (43)-(47).

To illustrate the interband mixing, introduced by an electric field, we show in Fig. 5 the conduction and the valence bands components of the WS wave functions, i.e., $\rho_v(x) = |\tilde{\phi}_v(x, k_y)|^2$ and $\rho_c(x) = |\tilde{\phi}_c(x, k_y)|^2$. The results are shown for one of the WS energy levels for a given electric field. The electric fields $F = 1.8 \text{ V/\AA}$ and $F = 3.6 \text{ V/\AA}$ are near $l = 2$ and $l = 1$ anticrossing points, respectively. In these cases, the interband mixing is strong and the electron densities in the conduction and the valence bands are comparable [see Fig. 5(a), (c)]. The spatial separation between the maxima of $\rho_v(x)$ and $\rho_c(x)$ is $\approx la$. Thus for $F = 1.8 \text{ V/\AA}$, i.e., $l = 2$, the distance between the maxima of ρ_v and ρ_c is $\approx 2a \approx 4.8 \text{ \AA}$, while for $F = 3.6 \text{ V/\AA}$, i.e., $l = 1$, the distance is $\approx a \approx 2.4 \text{ \AA}$.

For the electric field $F = 2.4 \text{ V/\AA}$, which is between $l = 1$ and $l = 2$ anticrossing points, the interband mixing is weak. In this case only the valence band component, ρ_v , is strong [see Fig. 5(b)].

In both cases, i.e., at the anticrossing points and away from them, the wave functions are localized in the x space. The localization length depends on the electric field. The points, at which the WS wave functions are localized, depends on the energy of the WS states. In Fig. 6 the total electron density, defined as $\rho(x) = \rho_v(x) + \rho_c(x)$, is shown for different WS states at electric field $F = 3.6 \text{ V/\AA}$, which correspond to $l = 1$ anticrossing point. With changing the energy of the WS state, the electron density distribution is shifted as a whole along the x axis.

C. Wannier-Stark states of two-band model: numerical results

In the previous section, analytical results for the WS spectra of the tight-binding model were obtained in the case of the δ -function dipole matrix elements. Such strong dependence of the dipole matrix element on the wave vector occurs near the Dirac points. Away from the

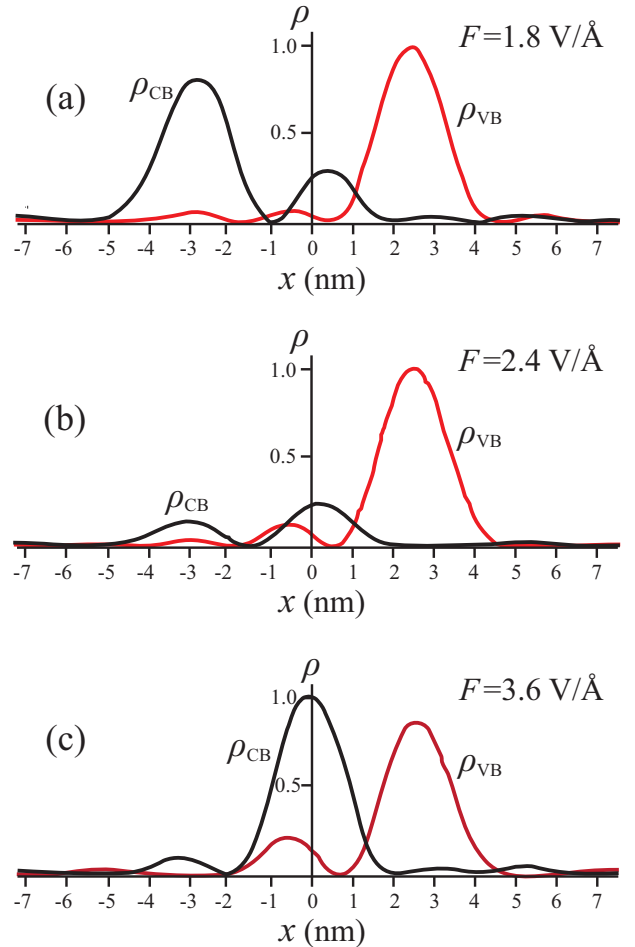


FIG. 5: Electron densities $\rho_v(x)$ and $\rho_c(x)$ in the conduction and valence bands of a given WS state. The electric field is (a) $F = 1.8 \text{ V/\AA}$, (b) $F = 2.4 \text{ V/\AA}$, (c) $F = 3.6 \text{ V/\AA}$. The fields 1.8 V/\AA and 3.6 V/\AA corresponds to $l = 2$ and $l = 1$ anticrossing points. The y component of the wave vector is $k_y = k_{y,0}$.

Dirac points, the dipole matrix element $|D_x|$ as a function of the wave vector has a broad peak. In this case the WS energy spectra can be obtained numerically.

It is convenient to solve the system of eigenvalue equations (8)-(9) by expanding the functions $\phi_v(\mathbf{k})$ and $\phi_c(\mathbf{k})$ in terms of the WS wave function of individual bands (14) and (20), calculated without interband coupling. Thus

$$\phi_v(\mathbf{k}) = \sum_n \mathcal{A}_n \phi_{v,n}^{(0)}(\mathbf{k}) \quad (49)$$

$$\phi_c(\mathbf{k}) = \sum_n \mathcal{B}_n \phi_{c,n}^{(0)}(\mathbf{k}), \quad (50)$$

where index n labels the WS states [see Eqs. (15) and (18)], \mathcal{A}_n and \mathcal{B}_n are expansion coefficients. Substituting expressions (49) and (50) into Eqs. (8)-(9) we obtain the system of eigenvalue equations on expansion coefficients

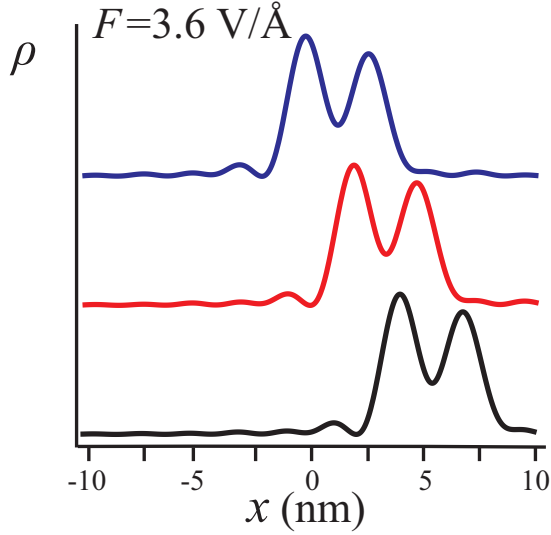


FIG. 6: Total electron density $\rho(x) = \rho_v(x) + \rho_c(x)$ of three WS states. The electric field is $F = 3.6$ V/Å and corresponds to $l = 1$ anticrossing point. The y component of the wave vector is $k_y = k_{y,0}$.

\mathcal{A}_n and \mathcal{B}_n

$$E\mathcal{A}_n = E_{v,n}^{WS}\mathcal{A}_n + F \sum_m \mathcal{D}_{nm}\mathcal{B}_n \quad (51)$$

$$E\mathcal{B}_n = E_{c,n}^{WS}\mathcal{B}_n + F \sum_m \mathcal{D}_{nm}^*\mathcal{A}_n, \quad (52)$$

where \mathcal{D}_{nm} are dipole matrix elements, calculated between the WS wave functions of individual bands,

$$\begin{aligned} \mathcal{D}_{nm} = & \left\langle \phi_{c,n}^{(0)} \left| D_x(\mathbf{k}) \right| \phi_{c,n}^{(0)} \right\rangle = \\ & \frac{1}{2k_0} \int_{-k_0}^{k_0} dk_x D_x(k_x, k_y) \exp \left[\frac{i}{eF} \left(2 \int_{-k_0}^{k_x} E_c(k', k_y) dk' \right. \right. \\ & \left. \left. + (E_{c,n}^{WS} - E_{v,m}^{WS})(k_x + k_0) \right) \right] \end{aligned} \quad (53)$$

In Fig. 7 the energy spectra of a finite size system of graphene, calculated numerically from the system of equations (49)-(50), are shown for different value of the y component of the wave vector, k_y . At $k_y = 0$ [see Fig. 7(a)] the system is far away from the Dirac points. In this case, the dipole matrix element as a function of k_x has a broad peak [see Fig. 3]. For $k_y = 0.32(2\pi/a)$ [see Fig. 7(b)], the system is close to the Dirac point with the dipole matrix element having a sharp δ -type peak. In this case, the values of the anticrossing gaps and the positions of the anticrossing points are close to the analytical expressions (41) and (42), obtained in the model with δ -function profile for the dipole matrix element.

The data, shown in Fig. 7, illustrate strong dependence of the spectra on the value of k_y , i.e. on the shape of the function $D_x(k_x)$. With increasing k_y , i.e. when the peak

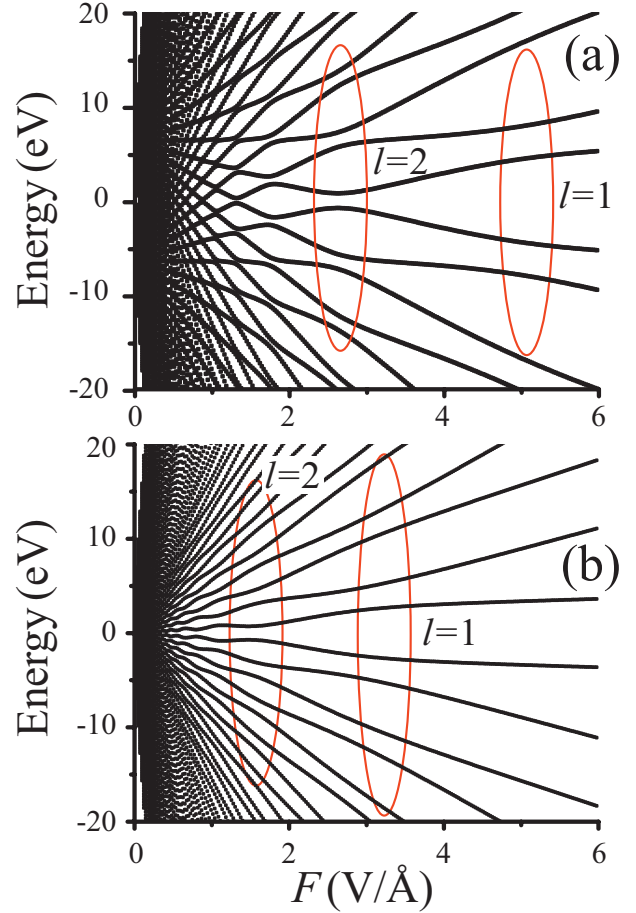


FIG. 7: Energy spectra of graphene in a constant electric field, parallel to the x axis. The spectra are calculated numerically for a finite size system for two values of k_y : (a) $k_y = 0$ and (b) $k_y = 0.32(2\pi/a)$. The number of states in each band is 100. The anticrossing points corresponding to $l = 1$ and $l = 2$ are marked by red lines.

in $D_x(k_x)$ becomes sharp, the anticrossing points move to smaller values of electric field and the anticrossing gaps become smaller. In Fig. 8, the anticrossing gaps and the positions of the anticrossing points are shown as a function of k_y for $l = 1$ and $l = 2$ anticrossing points. The general tendency is that with increasing k_y , both the anticrossing gaps, $\Delta_g^{(l)}$, and the electric fields, $F^{(l)}$, at which the anticrossing points are realized, are decreasing. The arrows in Fig. 7 show the analytical values of the anticrossing gaps and the positions of the anticrossing points, obtained from Eqs. (41) and (42). These values are close to the corresponding numerical parameters at $k_y = (1/3)(2\pi/a)$, i.e. near the Dirac point [see Fig. 7].

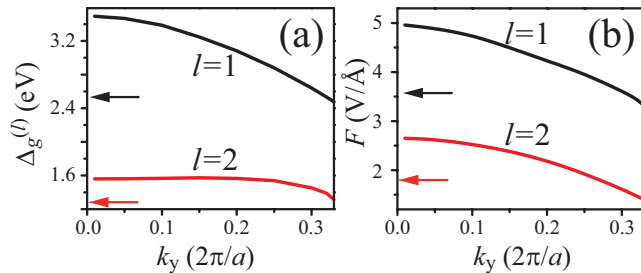


FIG. 8: (a) Anticrossing gaps, calculated at $l = 2$ and $l = 1$ anticrossing points, are shown as a function of the y component of the wave vector, k_y . (b) The positions of $l = 1$ and $l = 2$ anticrossing points are shown as a function of k_y . The electric field is parallel to the x axis.

D. Wannier-Stark states of two-band model: two Dirac points

By changing the direction of electric field, one can realize a situation when along a line of coupled states there are two Dirac points. For graphene, this happens for a line shown in Fig. 9(a), i.e. when the angle between the direction of electric field and axis x is 30° . Then for the line, shown in Fig. 9, we introduce one dimensional wave vector, κ , along the direction of electric field and write the dipole matrix element in terms of two δ -functions, localized at the Dirac points,

$$D_x(\kappa) = e\Lambda_1\delta(\kappa - \kappa_1) + e\Lambda_2\delta(\kappa - \kappa_2), \quad (54)$$

where κ_1 and κ_2 are the coordinates of the Dirac points along the line of coupled states. The wave vector κ changes from 0 to $\kappa_0 = (2\pi/a_\kappa)$, where $a_\kappa = 2\pi/\kappa_0$ determines the period of the system along the direction of electric field.

We follow the same steps as in the case of one Dirac point (see Sec. III B). Namely, we introduce three regions, $0 < \kappa < \kappa_1$, $\kappa_1 < \kappa < \kappa_2$, and $\kappa_2 < \kappa < \kappa_0$. In each region, the conduction and valence bands become decoupled and the wave functions have the form of Eqs. (24)-(25). At the boundary between the regions, i.e. at points $\kappa = \kappa_1$ and $\kappa = \kappa_2$, the boundary conditions have the form of Eqs. (28)-(29). Combining all these equations and taking into account the periodic boundary conditions at points $\kappa = 0$ and $\kappa = \kappa_0$ we obtain the following energy spectra of the coupled WS states

$$E_n^{(\pm)} = \pm \frac{eF}{\kappa_0} \left\{ \cos^{-1} \left[\cos \Lambda_1 \cos \Lambda_2 \cos \left(\frac{\kappa_0}{eF} \tilde{E}_{c,0} \right) - \sin \Lambda_1 \sin \Lambda_2 \cos \left(\frac{\kappa_0}{eF} \alpha \tilde{E}_{c,0} \right) \right] + 2\pi n \right\}. \quad (55)$$

Here $\tilde{E}_{c,0}$ is defined in terms of the linear integral over the line of coupled states (see Fig. 9),

$$\tilde{E}_{c,0} = \frac{1}{\kappa_0} \int_0^{\kappa_0} E_c(\kappa) d\kappa. \quad (56)$$

The coefficient $0 < \alpha < 1$ in Eq. (55) is defined through the following relation

$$\alpha = 1 - \frac{2}{\kappa_0 \tilde{E}_{c,0}} \int_{\kappa_1}^{\kappa_2} E_c(\kappa) d\kappa. \quad (57)$$

In dimensionless variables, $\varepsilon_n^{(\pm)} = E_n^{(\pm)}(\kappa_0/eF)$ and $\tilde{\varepsilon}_{c,0} = \tilde{E}_{c,0}(\kappa_0/eF)$, Eq. (55) becomes

$$\varepsilon_n^{(\pm)} = \pm \left\{ \cos^{-1} \left[\cos \Lambda_1 \cos \Lambda_2 \cos \tilde{\varepsilon}_{c,0} - \sin \Lambda_1 \sin \Lambda_2 \cos(\alpha \tilde{\varepsilon}_{c,0}) \right] + 2\pi n \right\}. \quad (58)$$

In Fig. 9(b) the dimensionless WS energy spectrum (58) is shown for parameters $\Lambda_1 = \Lambda_2 = \Lambda_0 = 0.6$ and $\alpha = 0.7$, which correspond to the graphene system. Specific feature of the spectrum is nonmonotonic dependence of the anticrossing gaps on the value of dimensionless band offset, $\tilde{\varepsilon}_{c,0}$. The gaps have both large and very small values. The positions of the anticrossing points are also irregular. The corresponding energy spectrum in the original units is shown in Fig. 9(c) as a function of electric field, F . The anticrossing gaps have nonmonotonic dependence on F . For example, the anticrossing gap at $l = 3$ is larger than the gap at $l = 2$. This behavior is different from the behavior of the anticrossing gaps of WS spectrum for a system, for which the dipole matrix elements are almost constant [15] or have a single peak as a function of the wave vector (see Sec. III B).

IV. CONCLUSION

Within a single (either conduction or valence) band approximation, the energy spectrum of an electron in graphene has a WS ladder structure with energy levels separated by the Bloch frequency, which is proportional to both the electric field and the lattice period of graphene crystal structure in the direction of electric field. In a two-band model, which is discussed above within the tight-binding nearest neighbor approximation, the electric field results in a mixing of the conduction and valence bands. As a result of such mixing, the energy spectrum of graphene as a function of electric field shows anticrossing points, which are characterized by the corresponding anticrossing gaps. The finite anticrossing gaps also illustrate that any constant electric field opens a gap in the energy dispersion of graphene. The magnitude of the gap depends on electric field.

The strength of the band mixing in an external electric field is determined by the magnitude of the interband dipole matrix element. In graphene, the dipole matrix elements have specific dependence on the electron wave vector. Namely, at the Dirac points, the dipole matrix elements have sharp peaks, i.e., in the reciprocal space, the interband coupling is strong only near the Dirac points.

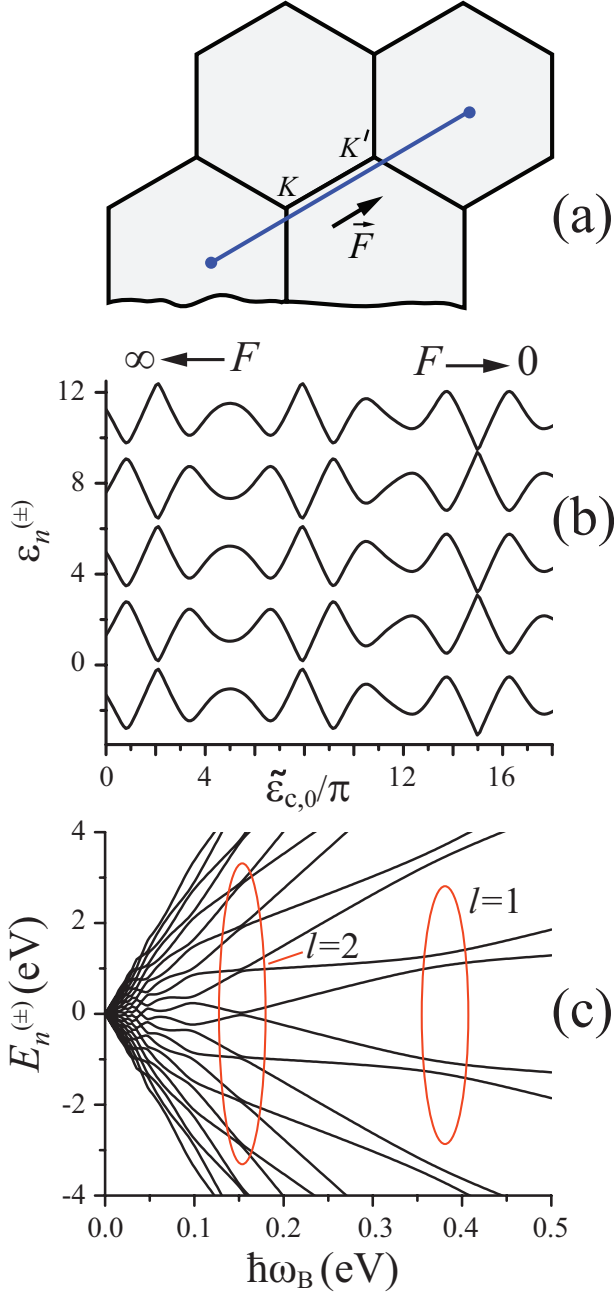


FIG. 9: (a) Line of coupled states in the reciprocal space is shown by blue solid line. Along this line there are two inequivalent Dirac points K and K' . The direction of electric field is also shown. (b) Dimensionless energies $\varepsilon_n^{(\pm)}$ of WS states, calculated from Eq. (58), are shown as a function of dimensionless parameter $\tilde{\varepsilon}_{c,0}$ for different values of integer number n . The parameters $\Lambda_1 = \Lambda_2 = \Lambda_0$ and α are $\Lambda_0 = 0.6$ and $\alpha = 0.7$. (c) The energies $E_n^{(\pm)}$ of the WS states, calculated from Eq. (55), are shown as a function of Bloch frequency, $\hbar\omega_B$, which is proportional to electric field. The anticrossing points, corresponding to $l = 1$ and $l = 2$, are marked by red lines. The parameters are $\Lambda_0 = 0.6$, $\alpha = 0.7$, and $E_{c,0} = 1$ eV.

In this case, approximating such strong dependence of the dipole matrix element on the wave vector by the δ -function, one can find analytical expression for the WS energy spectrum. Such analytical solution predicts both the positions of the anticrossing points and the corresponding anticrossing gaps. As a function of inverse electric field the anticrossing points are equidistant. In the dimensionless units (units of the Bloch frequency), the anticrossing gaps are the same at all anticrossing points. Thus, in the original energy units, the anticrossing gaps are proportional to electric field at the corresponding anticrossing points and, for graphene, have the following values $\Delta_g^{(l)} = (2.54/l)$ (eV), where $l = 1, 2, \dots$ is an integer. The largest anticrossing gap ≈ 2.54 eV corresponds to the anticrossing point $l = 1$ at the electric field ≈ 3.59 V/Å. In time-dependent electric field, when the electron dynamics is described in terms of the passage of the anticrossing points, the anticrossing gaps determine the characteristic time, $\tau_l = \hbar/\Delta_g^{(l)} = 0.26l$ fs, which characterizes the adiabatic dynamics. Namely, if time τ_p of passage of an anticrossing point, which is also the characteristic time of variation of electric field, is much larger than τ_l , $\tau_p \gg \tau_l$, then the electron dynamics is adiabatic. For example, if $\tau_l \approx 1$ fs, then the passages of anticrossing points $l = 1$ and 2 with the characteristic times $\tau_l = 0.25$ fs and 0.51 fs are adiabatic, while the passages of the points $l > 2$ is diabatic.

Acknowledgment

This work was supported by MURI grant N00014-13-1-0649 from the US Office of Naval Research, grant No. DE-FG02-11ER46789 from the Materials Sciences and Engineering Division, Office of the Basic Energy Sciences, Office of Science, U.S. Department of Energy, Grant No. DE-FG02-01ER15213 from the Chemical Sciences, Biosciences and Geosciences Division, Office of the Basic Energy Sciences, Office of Science, U.S. Department of Energy, and NSF grant No. ECCS-1308473. MIS gratefully acknowledges also support by the Max Planck Society and the Deutsche Forschungsgemeinschaft Cluster of Excellence: Munich Center for Advanced Photonics (<http://www.munich-photonics.de>) during his Sabbaticals at Munich.

-
- [1] F. Bloch, *Z. Phys. A* **52**, 555 (1929).
- [2] C. Zener, *Proc. Royal Soc. A* **145**, 523 (1934).
- [3] G. H. Wannier, *Elements of Solid State Theory* (Cambridge University Press, Cambridge, England, 1959).
- [4] G. H. Wannier, *Phys. Rev.* **117**, 432 (1960).
- [5] J. Bleuse, G. Bastard, and P. Voisin, *Phys. Rev. Lett.* **60**, 220 (1988).
- [6] E. E. Mendez, F. Agullo-Rueda, and J. M. Hong, *Phys. Rev. Lett.* **60**, 2426 (1988).
- [7] J. Feldmann, K. Leo, J. Shah, D. A. B. Miller, J. E. Cunningham, T. Meier, G. von Plessen, A. Schulze, P. Thomas, and S. Schmitt-Rink, *Phys. Rev. B* **46**, 7252 (1992).
- [8] E. E. Mendez and G. Bastard, *Phys. Today* **46**, 34 (1993).
- [9] T. Dekorsy, P. Leisching, C. Waschke, K. Kohler, K. Leo, H. G. Roskos, and H. Kurz, *Semicond. Sci. Tech.* **9**, 1959 (1994).
- [10] O. Schubert, M. Hohenleutner, F. Langer, B. Urbanek, C. Lange, U. Huttner, D. Golde, T. Meier, M. Kira, S. W. Koch, et al., *Nat. Photon* **8**, 119 (2014), ISSN 1749-4885.
- [11] A. Di Carlo, P. Vogl, and W. Ptz, *Phys. Rev. B* **50**, 8358 (1994), pRB.
- [12] B. Rosam, K. Leo, M. Glck, F. Keck, H. J. Korsch, F. Zimmer, and K. Khler, *Phys. Rev. B* **68**, 125301 (2003).
- [13] G. Markus, R. K. Andrey, and H. J. Korsch, *J. Opt. B: Quantum Semiclass. Opt.* **2**, 694 (2000).
- [14] M. Gluck, A. R. Kolovsky, and H. J. Korsch, *Phys. Rep.* **366**, 103 (2002), ISSN 0370-1573.
- [15] V. Apalkov and M. I. Stockman, *Phys. Rev. B* **86**, 165118 (2012).
- [16] A. Schiffrin, T. Paasch-Colberg, N. Karpowicz, V. Apalkov, D. Gerster, S. Muhlbrandt, M. Korbman, J. Reichert, M. Schultze, S. Holzner, et al., *Nature* **493**, 70 (2012).
- [17] M. Schultze, E. M. Bothschafter, A. Sommer, S. Holzner, W. Schweinberger, M. Fiess, M. Hofstetter, R. Kienberger, V. Apalkov, V. S. Yakovlev, et al., *Nature* **493**, 75 (2012).
- [18] A. K. Geim and K. S. Novoselov, *Nat. Mater.* **6**, 183 (2007).
- [19] A. H. C. Neto, F. Guinea, N. M. R. Peres, K. S. Novoselov, and A. K. Geim, *Rev. Mod. Phys.* **81**, 109 (2009).
- [20] D. S. L. Abergel, V. Apalkov, J. Berashevich, K. Ziegler, and T. Chakraborty, *Adv. Phys.* **59**, 261 (2010).
- [21] A. R. Kolovsky and E. N. Bulgakov, *Phys. Rev. A* **87**, 033602 (2013).
- [22] P. Wallace, *Phys. Rev.* **71**, 622 (1947).
- [23] J. Slonczewski and P. Weiss, *Phys. Rev.* **109**, 272 (1958).
- [24] R. Saito, G. Dresselhaus, and M. Dresselhaus, *Physical Properties of Carbon Nanotubes* (Imperial College Press, London, 1998).
- [25] S. Reich, C. Thomsen, and J. Maultzsch, *Carbon Nanotubes* (Wiley-VCH, Weinheim, 2004).